Carbon 139 (2018) 1126–1135

Contents lists available at ScienceDirect

Carbon

journal homepage: www.elsevier.com/locate/carbon

Ultralight, highly compressible and fire-retardant graphene aerogel with self-adjustable electromagnetic wave absorption

Zicheng Wang [a, f], Renbo Wei [a, *], Junwei Gu [b], Hu Liu [c, f], Chuntai Liu [c], Chunjia Luo [b], Jie Kong [b, ***], Qian Shao [d], Ning Wang [e], Zhanhu Guo [f, ****], Xiaobo Liu [a, **]

[a] Research Branch of Advanced Functional Materials, School of Materials and Energy, University of Electronic Science and Technology of China, Chengdu, 611731, PR China
[b] MOE Key Laboratory of Material Physics and Chemistry Under Extraordinary Conditions School of Science, Northwestern Polytechnical University, Xi'an, 710072, PR China
[c] National Engineering Research Center for Advanced Polymer Processing Technology, Zhengzhou University, Zhengzhou, Henan 450002 PR China
[d] College of Chemical and Environmental Engineering, Shandong University of Science and Technology, Qingdao, Shandong Province, 266590, PR China
[e] State Key Laboratory of Marine Resource Utilization in South China Sea, Hainan University, Haikou 570228, PR China
[f] Integrated Composites Laboratory (ICL), Department of Chemical & Biomolecular Engineering, University of Tennessee, Knoxville, TN 37996, USA

ARTICLE INFO

Article history:
Received 22 May 2018
Received in revised form
10 July 2018
Accepted 6 August 2018
Available online 7 August 2018

ABSTRACT

Macroscopic three-dimensional (3D) free-standing porous all-graphene aerogel with ultralight density and high compressibility is successfully fabricated through a mild in-situ self-assembly and thermal annealing processes. The formed interconnected 3D porous graphene network, high thermal stable all-graphene composition and large porosity of aerogels made it possible to remove heat quickly during combustion, exhibiting a conspicuous fire-retardancy. Meanwhile, excellent recoverable compressibility with high strain levels of up to 75% endowed the aerogel with high sensitive strain-responsive characteristic in volume electrical conductivity, thereby opening a new way for realizing the adjustment of internal free space and electrical conductivity of 3D architecture. Based on the results, the microwave absorption performance of the graphene aerogel was effectively self-adjusted via a simple mechanical compression. The optimal absorbing value was up to 61.09 dB with a broad qualified bandwidth of 6.30 GHz at the thickness of 4.81 mm when the compression strain ratio of the sample was controlled to be 30%.

1. Introduction

With extensive applications of electronic communication technology, especially the pervasive diffusion of broadband, multiband and high-power electronic facilities including satellite communication, wide band radar, wireless network, and portable digital hardware, designing and fabricating new high-performance microwave absorption materials to protect electronic devices and human being from undesirable electromagnetic interference (EMI) and radiation pollution becomes a significant concern in contemporary society. Meanwhile, extending frequency range from radio frequency up to a few tens of gigahertz and the increasing demand for electronic devices integrating smartness and multifunctionality are further pushing the development of innovative microwave absorption materials with broadband, lightweight, low cost, high thermal stability and high corrosion resistance in harsh environments. To date, various nanomaterials, especially carbon-based composites as an alternative candidate to ponderous ferrites, metallic magnets, ceramics, and their hybrids, have been successfully prepared and exhibit excellent microwave absorption performance [1–5]. Among them, graphene-based composites attract increasing interests and become more promising as a novel microwave absorption material due to stable two-dimensional (2D) carbon nanostructure, high specific surface area, and low density apart from excellent electrical conductivity.

As reported by previous literature, most of works were mainly concentrated on fabrication of graphene and inorganic magnetic

* Corresponding author.
** Corresponding author.
*** Corresponding author.
**** Corresponding author.
E-mail addresses: weirb10@uestc.edu.cn (R. Wei), kongjie@nwpu.edu.cn (J. Kong), zguo10@utk.edu (Z. Guo), liuxb@uestc.edu.cn (X. Liu).

https://doi.org/10.1016/j.carbon.2018.08.014
0008-6223/

hybrid materials with special electromagnetic properties [6–9] and/or dispersing graphene-based hybrids into polymeric matrixes to form effective conductive network [10–16], thereby attenuating electromagnetic irradiation. However, the characteristics of large loading content, high density, poor thermal stability and low corrosion resistance hindered their practical applications severely due to the introduction of lumpish magnetic particles and/or unstable polymeric matrixes. On the other hand, the goodish microwave absorbing performance of those composites was primarily attributed to the conventional impedance match between dielectric loss and magnetic loss and/or sole Debye relaxation between graphene sheets and polymeric matrixes. Few of novel explorations were attempted to solve the existing drawbacks.

Recently, significant progresses have been made toward fabricating macroscopic 3D graphene architectures from 2D graphene sheets [17–20]. As reported by the literature, the formation of porous graphene network endows 3D architectures with large internal free space, which can substantially improve the random multiple reflection of electromagnetic wave entering the architectures at the internal interfaces of the closed cell wall due to the impedance mismatching between air and graphene sheets, thereby enhancing the final absorption of electromagnetic wave effectively. However, the adjustment of their performance is almost limited in either renewedly preparing a sample with big thickness or high loading content, or unhandily stacking the thin samples to form a thicker one [17–19]. Further researches in clarifying the effects of free space and electrical conductivity of 3D graphene architecture on microwave absorption are rarely reported [20]. Furthermore, for 3D-PPy/RGO reported by Wu [17], the existence of polypyrrole (PPy) endowed the aerogel with a high density (~140 mg/cm^3) and poor thermal stability, which impaired its portability and further application in harsh environments. More importantly, high pressure during solvothermal process and high-temperature annealing treatment ($\geqq$ 600 °C) significantly increase the cost and limit its preparation and application on a large scale [18,20].

In this study, we report a facile, low-cost and large-scale approach to fabricate 3D free-standing all-graphene aerogels with any shapes, ultra-low density, fire retardancy, and high recyclable compressibility via in situ self-assembly of 2D graphene sheets under atmospheric pressure and then cost-effective annealing treatment. The excellent compressibility endows the graphene aerogel with remarkable strain-responsive characteristic, thereby realizing the adjustment of internal free space and electrical conductivity of 3D architectures through a simple mechanical compression. As a result, the final microwave absorption performance of graphene aerogel can be efficiently self-adjusted and achieves the optimal absorbing value of 61.09 dB with a broad qualified frequency bandwidth ($\leq$-10 dB) of 6.30 GHz at the thickness of 4.81 mm when the compression strain of the sample is controlled to be 30%.

2. Experimental

2.1. Materials

Graphite powders (325 mesh) were obtained from Qingdao Jin Ri Lai Graphite Co. Ltd. (Qingdao, China). Sodium hydrogen sulfite ($NaHSO_3$, Analytical grade) was purchased from Tianjin BODI chemicals (Tianjin, China) and used without any further purification.

2.2. Synthesis of reduced graphene oxide (RGO) Aerogel and Graphene Aerogel

Graphene oxide (GO) was prepared from graphite powder through an improved Hummer's method as reported [21]. The obtained GO was homogeneously dispersed into deionized water (4.0 mg/mL) by vigorous stirring and sonication for 20 min at ambient temperature. $NaHSO_3$ (20 mg) was subsequently added into the brown dispersions. After stirring, the homogeneous suspension (10 mL) was sealed in a glass vial (20 mL) and heated at 80 °C for 24 h without stirring. Then, the as-prepared RGO hydrogel was dialyzed with deionized water to remove residual $NaHSO_3$ and other ions. For aerogel preparation, the RGO hydrogel was freeze-dried to remove the remaining water inside. The corresponding product was denoted as RGO Aerogel. To further improve the reduction degree of GO, the resultant aerogel was annealed at 230 °C for 2 h, and the final product was labeled as Graphene Aerogel. Furthermore, in order to investigate the self-assembly behavior from GO to RGO, the reaction mass ratios between GO and $NaHSO_3$ were controlled at 1:1.5, 1:1, 1.5, and 2:1 by using similar procedures and conditions. The corresponding products were named as RGO-1:1.5 Aerogel, RGO-1:1 Aerogel, RGO-1.5:1 Aerogel and RGO-2:1 Aerogel (RGO Aerogel as a reference without special emphasis), respectively.

2.3. Characterizations

Scanning electron microscopic (SEM) images were taken on a JSM 6490LV (JEOL, Japan) field emission microscope. Thermal gravimetric analyzer (TGA) analysis was carried out by using TA Q50 system under nitrogen atmosphere at a heating rate of 20 °C/min. Ultraviolet–visible spectrophotometer (UV–Vis) spectra were obtained on a UV2501-PC spectrophotometer. X-ray diffraction (XRD) was recorded on a RINT 2400 vertical goniometer (Rigaku, Japan) with Cu K_α radiation. Raman spectra were recorded on a Renishaw Invia Raman Microprobe using a 532 nm argon ion laser. X-ray photoelectron spectroscopy (XPS) measurements were carried out on ESCA 2000 (VG Microtech, UK) using a monochromic Al Kα ($h\nu = 1486.6$ eV) X-ray source. The infrared image in a temperature gradient of Graphene Aerogel was recorded with a thermal camera (Ti 200, Fluke, USA).

Mechanical properties of aerogels were measured by using a SANS CMT6104 series desktop electromechanical universal testing machine equipped with two flat-surface compression stages and 100 N load cells. The top and bottom surfaces of cylindrical aerogel were coated with a uniform layer of silver paste. The cylindrical samples were circularly compressed to the maximum restorable compression strain at a speed of 125 mm/min for the tests. Meanwhile, the stainless steel stages were also connected with a precision digital resistor (Agilent 2901, California, USA) in series. The universal mechanical testing machine and the precision digital resistor were coupled in parallel to record the piezoresistive behavior online. The sampling rate was controlled at 0.2 Hz in piezoresistive testing. The electromagnetic parameters of the aerogels with different compression strains were measured on a vector network analyzer (Agilent 8720ET) at 0.5–18 GHz. The paraffin was used as a supporting matrix to immobilize the aerogels under a certain compression strain. And the original thickness of RGO Aerogel and Graphene Aerogel were 6.91 mm and 6.87 mm, respectively. The test samples were fabricated by vacuum-impregnating the compressed aerogel with melting paraffin and cut into standard coaxial rings with an outer diameter of 7.0 mm, an inner diameter of 3.0 mm.

3. Results and discussion

3.1. Fabrication of reduced graphene oxide aerogels

The fabrication procedure of the macroscopic free-standing all-

graphene 3D architecture with a cylindrical morphology was illustrated in Fig. 1A. The hydrophilic GO powder can be well dispersed in water to form a stable suspension. $NaHSO_3$ was selected as reducing agent for the in-situ reduction of GO in this system. With the reaction proceeding at 80 °C under atmospheric pressure, GO sheets are gradually reduced, leading to the increase of hydrophobicity in the surface of GO sheets and the enhancement of π-π interaction between adjacent graphene sheets. At the end, the cylindrical 3D reduced graphene oxide (RGO) hydrogel can be successfully fabricated in a glass vial through the synergistic effect between aggregation and steric hindrance of graphene sheets. However, too many defects in them make it difficult to get a facile, low-cost and large-scale approach to construct the macroscopic free-standing all-graphene 3D architecture with ultralight density and high recyclable compressibility. In this paper, a lot of optimizing explorations have been devoted to the fabrication and freezing-dry process of RGO hydrogel for realizing high compressibility of the final aerogels. The final RGO Aerogel can be easily obtained by freeze-drying process to remove the remaining water inside. Meanwhile, the self-assembly behavior from GO to RGO can be controlled by tuning the reaction mass ratios between GO and $NaHSO_3$ under similar procedures and conditions. As shown in Fig. 1B, the density of RGO aerogels is calculated and exhibits a tendency to gradually decrease from 16.7 to 6.4 mg/cm^3 as the loading content of reductant decreases, which can be regarded as a consequence of immoderate stacking of reduced graphene sheets under high concentration of reductant. Similar to other reports about 3D architectures fabricated by the self-assembly of graphene sheets and additives (hexamethylenetetramine [22], ethylenediamine [23], and carbon nanotubes [24]), when the reaction mass ratio is 2:1, the density of the graphene aerogel can also reach the ultralow density range of below 10 mg/cm^3, which is comparable to the density of air at room temperature. The ultralow density of RGO Aerogel can be attributed to the formation of cross-linked microcellular structure with cell size beyond several tens microns in the 3D architecture, as shown in the cross-sectional SEM micrograph (Fig. 1E and F), leading to a large amount of air included in the pores. As demonstrated in Fig. 1C, the ultralight RGO-2:1 Aerogel (RGO Aerogel as default) can be supported by standing on a soft feather without any destruction, which once again verifies the ultralow density of RGO Aerogel.

Moreover, the formation of cross-linked 3D architecture successfully endows RGO Aerogel with excellent compressibility. As demonstrated in Movie S1, the cylindrical RGO Aerogel can be circularly compressed to a large strain and is still able to almost completely recover to its original shape rapidly after the loading is released. As a result of the precise uniaxial compression test, the maximum recoverable strain (ε) of the as-prepared RGO Aerogel is up to 75% as shown in Fig. 1D. Similar to other reports about compressible structures [23–26], the compression rebound curve also shows an initial linear region at $\varepsilon < 10\%$, a plateau with a gradually increasing slope, and a quick increase in the stress until the strain up to 75% while the stress under releasing rapidly decreases to zero ($\varepsilon = 0\%$), corresponding to the complete recovery of RGO Aerogel in volume. More importantly, the preparation of RGO hydrogel can be successfully carried out on a large scale by using the same method. Meanwhile, the as-prepared RGO hydrogel is good in mechanical properties which can be cut into small monoliths with any shapes by a knife. The obtained final RGO aerogels also exhibit ultralow density and excellent compressibility as

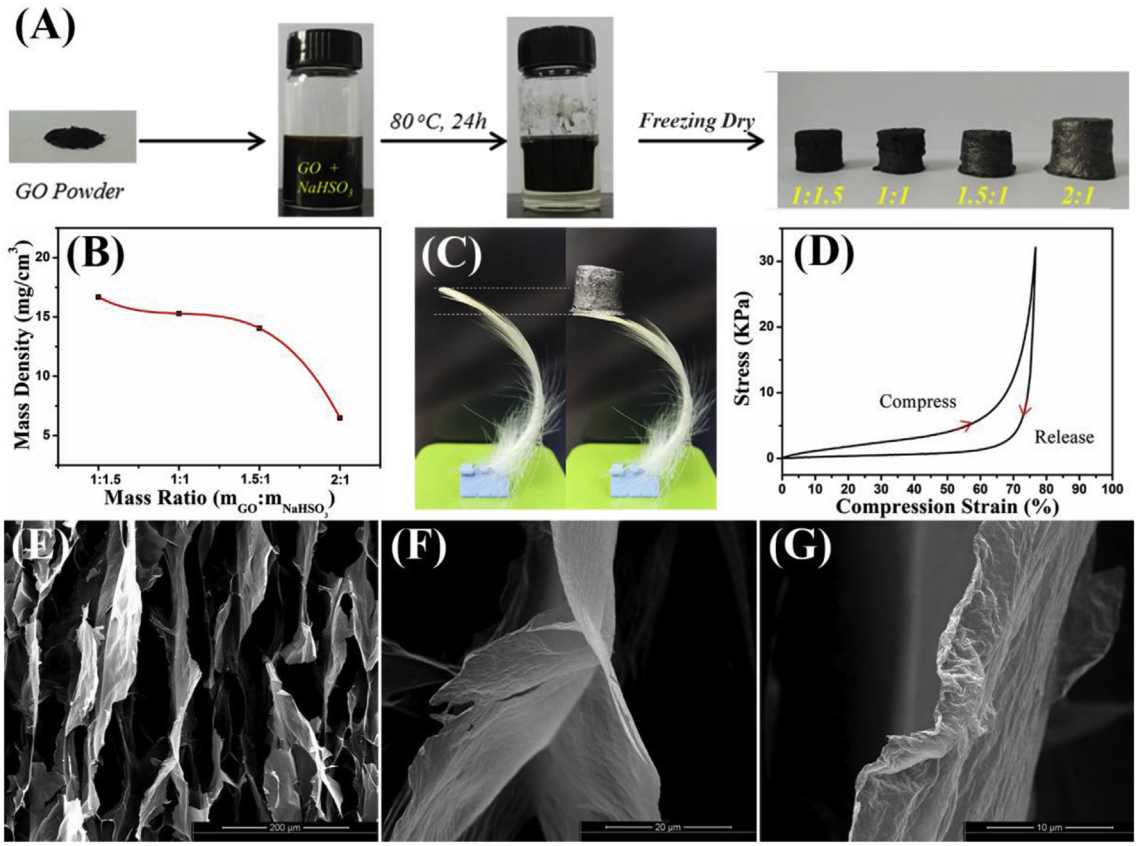

Fig. 1. (A) Images of the fabrication process of RGO aerogels via a mild in-situ self-assembly of GO with different loading contents of $NaHSO_3$ as reducing agent. (B) The density of RGO aerogels as a function of the original mass ratio between GO and $NaHSO_3$. (C) Ultralight RGO-2:1 Aerogel standing on a soft feather. (D) Compressive stress-strain curve of RGO-2:1 Aerogel. (E–G) SEM images of cross-section morphology of RGO-2:1 Aerogel. (A colour version of this figure can be viewed online.)

shown in Fig. S1, which make it possible to become a practical approach with a distinct competitive advantage for fabricating the macroscopic free-standing all-graphene 3D architecture with any shapes.

Supplementary data related to this article can be found at https://doi.org/10.1016/j.carbon.2018.08.014.

3.2. Structural characterization of RGO Aerogel and Graphene Aerogel

In order to obtain more information during the self-assembly process, TGA was employed to explore the microstructural changes of GO sheets in fabricating 3D aerogels. For GO, the decomposition of oxygen functional groups within graphene sheets can be attributed to a range of temperatures depending upon a number of factors including synthesis method for GO. As shown in Fig. 2A(a), the original GO shows a sharp weight loss of ~35% at the temperature range from 230 °C, which can be attributed to the decomposition of labile oxygen functional groups of GO sheets [27]. After reacting with $NaHSO_3$, the obtained RGO Aerogel (Fig. 2A(b)) exhibits a higher thermal stability, indicating that $NaHSO_3$ successfully realizes the reduction of GO sheets, and prevents dramatic weight loss at low temperatures. However, a nonnegligible weight loss (~15% below 300 °C) in the curve of RGO Aerogel suggests that further thermal annealing is indispensable for removing the residual oxygen functional groups in graphene sheets. After further thermal annealing at 230 °C for 2 h, the weight loss of as-prepared Graphene Aerogel is only ~3% before 500 °C (Fig. 2A(c)), which verifies the efficiency of the thermal reduction for RGO Aerogel.

To further monitor the self-assembly process of GO, UV–Vis spectra were also utilized to trace the changing interaction between graphene sheets. As shown in Fig. 2B(a), the initial GO homogeneously dispersed in water displays a distinct absorption peak at 227 nm and a weak shoulder peak at 301 nm, corresponding to $\pi \rightarrow \pi^*$ transitions of aromatic C=C bonds and $n \rightarrow \pi^*$ transitions of C=O bonds, respectively [28]. After reacting with $NaHSO_3$, the characteristic absorption peak of C=C bonds of the as-prepared RGO hydrogel is red-shifted to 264 nm, whereas the shoulder peak of C=O bonds disappears (Fig. 2B(b)). This can be ascribed to the restoration of π-conjugated network within graphene sheets and breakaway of C=O bonds in graphene sheets, respectively, which once again confirm that GO is successfully and effectively reduced by $NaHSO_3$ [29]. Furthermore, the restoration of π-conjugated network within graphene sheets will further improve the π-π interaction between graphene sheets, thereby promoting the fabrication of interconnected 3D graphene network (RGO hydrogel). However, for RGO Aerogel (Fig. 2B(c)), the remarkable absorption peak of C=C bonds disappears completely, suggesting a significant structural change during the freeze-drying process from hydrogel to aerogel. It may be attributed to the fact that the growth of ice crystals during the freeze-drying process will further push the adjacent RGO sheets to form a microcosmic stacking structure as the cell wall of microcellular cavity (Fig. 1G) [22], leading to the disappearance of the characteristic absorption peak of C=C bonds in graphene sheets. As a result, the enhanced π-π interaction between graphene sheets and the formed stacking structure synergistically endow the 3D architecture with excellent mechanical properties as demonstrated in Movie S1. Meanwhile, similar phenomena can be observed in the curve of Graphene Aerogel (Fig. 2B(d)).

To further probe the surface chemical changes during the self-assembly and thermal annealing processes, the samples were also characterized by XPS. As displayed in Fig. S2A, the XPS spectra of the samples as predicted exhibit two distinct peaks centered at 287 and 534.5 eV, corresponding to C 1s and O 1s, respectively. Moreover, it can be clearly observed that the carbon content of the samples gradually increases while the oxygen content decreases accordingly after the self-assembly and thermal annealing processes. As calculated in Table S1, the area ratio of C 1s to O 1s peak (C/O ratio) of GO gradually increases from 2.04 to 3.32 (RGO

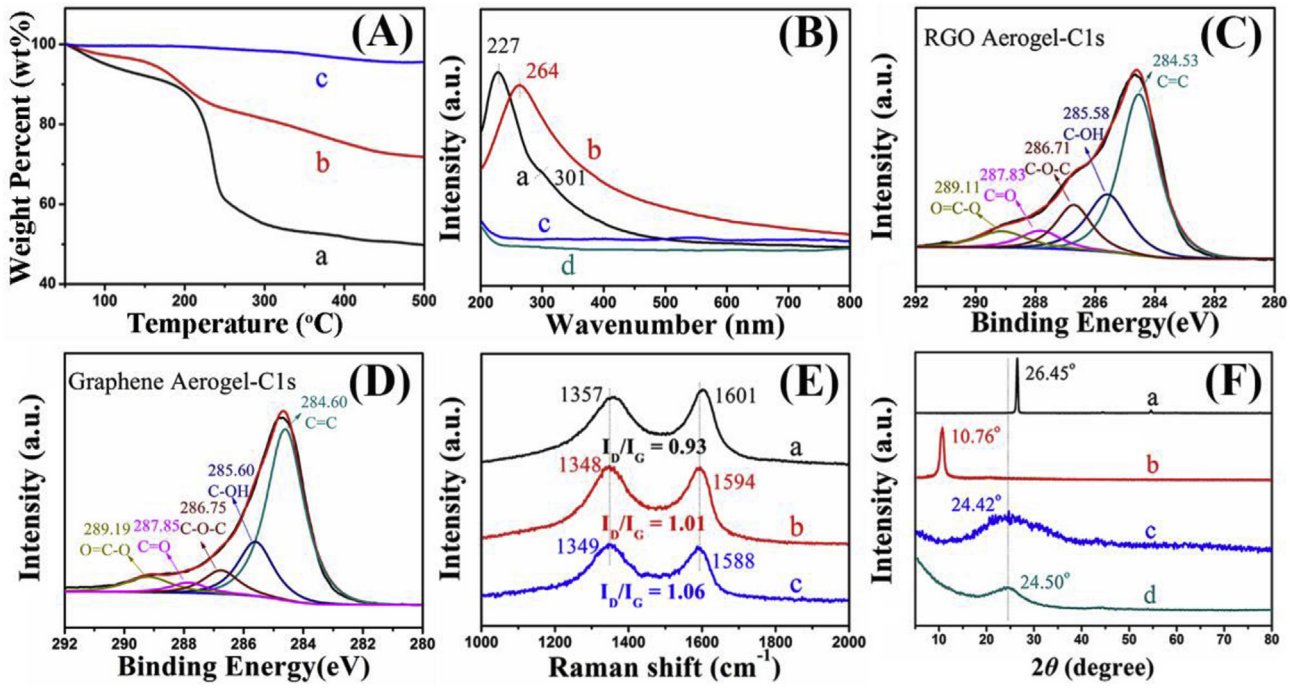

Fig. 2. (A) TGA curves of (a) GO, (b) RGO Aerogel and (c) Graphene Aerogel. (B) UV–vis spectra of (a) GO, (b) RGO hydrogel, (c) RGO Aerogel and (d) Graphene Aerogel dispersed in water. (C, D) High-resolution C1s XPS spectra of RGO Aerogel and Graphene Aerogel. (E) Raman spectra of (a) GO, (b) RGO Aerogel and (c) Graphene Aerogel. (F) XRD patterns of (a) original Graphite, (b) GO, (c) RGO Aerogel and (d) Graphene Aerogel. (A colour version of this figure can be viewed online.)

Aerogel), and then to 5.16 (Graphene Aerogel), which once again confirms the efficiency in reduction of GO during the self-assembly and thermal annealing processes. Furthermore, the C 1s spectrum of GO in high-resolution could be quantitatively differentiated into five different carbon species located at 289.21 (O═C–O), 287.90 (C═O), 286.85 (C–O–C), 285.63 (C–OH), and 284.38 eV (C═C/C–C) as shown in Fig. S2B [30]. After self-assembly process, the intensity of C–O–C and C═O peak in RGO Aerogel significantly decreases as compared to that of GO (Fig. 2C and Table S2), revealing a fact that epoxy and carbonyl groups on the surface of GO have been effectively consumed by the reductant, which is consistent with the result of UV–Vis spectra (Fig. 2B). As for Graphene Aerogel, further decreased intensity of C–O–C and C═O peak is also observed in Fig. 2D, which once again confirms that thermal annealing process is an effective and powerful method for facilitating further degradation of residual oxygen functional groups on graphene sheets.

In addition, significant structural changes that occur in graphene frameworks during the self-assembly and thermal annealing processes can be also reflected by Raman spectra. As shown in Fig. 2E(a), GO exhibits typical Raman spectra of graphitic structure with two conspicuous peaks at ~1357 cm^{-1} (D band) and ~1601 cm^{-1} (G band), corresponding to the structural defects and/or partially disordered structures of sp^2 carbon domains, and the E_{2g} vibration mode of the sp^2 domains, respectively [31]. In comparison with GO, it can be obviously observed that the peak of aerogels at G band is gradually down-shifted to 1594 cm^{-1} (RGO Aerogel), and then to 1588 cm^{-1} (Graphene Aerogel), which can be attributed to the recovery of the hexagonal network of carbon atoms with defects [31]. Such results once again confirm the efficient reduction of GO. Meantime, the intensity ratio of the D to G peak (I_D/I_G) displays a tendency to increase from 0.93 to 1.01, and 1.06. According to the modified Tuinstra-Koenig model [32], the in-plane nanocrystalline size (L_a) can be estimated by an empirical relation L_a [nm] = $(2.4 \times 10^{-10})\ \lambda^4 (I_D/I_G)^{-1}$. The changes suggest that the self-assembly and thermal annealing processes gradually alter the framework of GO sheets with smaller π-conjugated sp^2 domains in size, but more in number.

The identification of GO to graphene aerogel was also carried out by an X-ray diffraction (XRD). As shown in Fig. 2F(a) and 2F(b), the initial GO powder as compared with the natural graphite (d-spacing 3.37 Å at $2\theta = 26.45°$) shows a well-defined diffraction peak indexed to (001) centered at 10.76°, corresponding to a d-spacing of 8.22 Å [33]. The 4.85 Å expansion of d-spacing mainly originates from the effective intercalation of oxygen-functional groups into graphite interlayers, thereby achieving the complete exfoliation of graphene sheets. For RGO Aerogel (Fig. 2F(c)), the characteristic diffraction peak (001) of GO completely disappears, while a new broad diffraction peak at 24.42° with a d-spacing of 3.64 Å arises, corresponding to the (002) planes of graphene [34,35]. The drastic contrast in XRD patterns once again confirms the removal of oxygen-functional groups from GO sheets and restoration of the graphitic structure [36]. Meanwhile, the decreased interlayer spacing suggests that a reversal self-assembly of the as-formed graphene sheets occurs, resulting in the formation of interconnected 3D graphene network. Furthermore, as for Graphene Aerogel (Fig. 2F(d)), the stacking peak (002) of graphene is further up-shifted to 24.50° with a narrower full width at half maxima (FWHM), which is closer to the typical peak of pristine graphite. According to Scherrer formula, the narrower full width at half maxima (FWHM) is the higher stacking height (L_c) of graphene layers in the c-direction. The increase of stacking height for Graphene Aerogel can be assigned as a result of the further enhancement of π-π interaction between graphene sheets. This indirectly confirms that thermal annealing process can effectively promote the further restoration of π-conjugated network within graphene sheets and the formation of graphene stacking structure at high temperature. As a result, macroscopic interconnected graphene 3D architecture can be successfully fabricated through a mild in-situ self-assembly and indispensable thermal annealing processes.

3.3. Fire-retardancy and piezoresistive behavior of RGO Aerogel and Graphene Aerogel

In this study, the effective fabrication of interconnected porous all-graphene architecture endows the final aerogel with ultralow density and excellent compressibility as shown in Fig. 1. Moreover, the high thermally stable all-graphene composition and large porosity of aerogels make it possible to become a potential fire-retardant material, which will further extend the application in microwave absorption. As predicted, the aerogel exhibits excellent fire retardancy when exposed to the flame of an alcohol burner and cannot be lit even heated to glowing as demonstrated in Fig. 3A and Movie S2. In order to further explore the fire-retardant mechanism of the aerogel, the sample was placed on a 400 °C heating stage for 1 h (Fig. S3). And the infrared image of Graphene Aerogel was recorded with a thermal camera (Ti 200, Fluke, USA). As shown in Fig. 3B, the corresponding thermal infrared image exhibits a distinct temperature gradient and maintains a relatively low temperature of about 69 °C on the top surface of Graphene Aerogel with a thickness of 1.5 cm, which is similar to that of ZrO_2 sponge [37]. According to the result, it can be concluded that the existence of high porosity in the all-graphene aerogel can effectively facilitate the quick removal of heat during combustion, thereby endowing Graphene Aerogel with excellent fire-retardancy.

Supplementary data related to this article can be found at https://doi.org/10.1016/j.carbon.2018.08.014.

On the other hand, due to the formed interconnected 3D conductive graphene network with high porosity, excellent recoverable compressibility under high strain levels up to 75% will bring a unique strain-responsive characteristic between electrical conductivity and applied compression strain. As demonstrated in Fig. 3C and Movie S3, when the aerogel is connected in series by two conductive indium tin oxide (ITO) plates with a battery and a lamp to form a simple circuit, the brightness of the lamp can be directly controlled by compressing Fig. 3C(a-c) or releasing (Fig. 3C(d)) the aerogel, showing a promising potential as a large-scale strain sensor. In order to further quantitatively investigate the strain-sensing behavior of the aerogels, the universal mechanical testing machine (SANS CMT6104) and the precision digital resistor (Agilent 2901) were coupled in parallel to simultaneously record the stress-strain curves and the corresponding piezoresistance of the aerogels (as illustrated in Fig. S4A and S4B). As displayed in Movie S4 and Fig. S4C, the aerogels can be cyclically compressed and released without any impairment in the maximum recoverable strain range of 0%–75% up to 10 cycles, indicating excellent compression reproducibility. Meanwhile, in the stress-strain curves, it is worth noting that the compression stress of Graphene Aerogel (Fig. S4C(b)) under the same compression strain exhibits a significant decrease as compared to that of RGO Aerogel (Fig. S4C(a)), which may be attributed to the internal stress-relieving during the thermal reduction process.

Supplementary data related to this article can be found at https://doi.org/10.1016/j.carbon.2018.08.014.

At the same time, the piezoresistance response of the aerogels was also traced in situ during the compression-recovery process. The corresponding volume electrical conductivity can be calculated by using Equation (1):

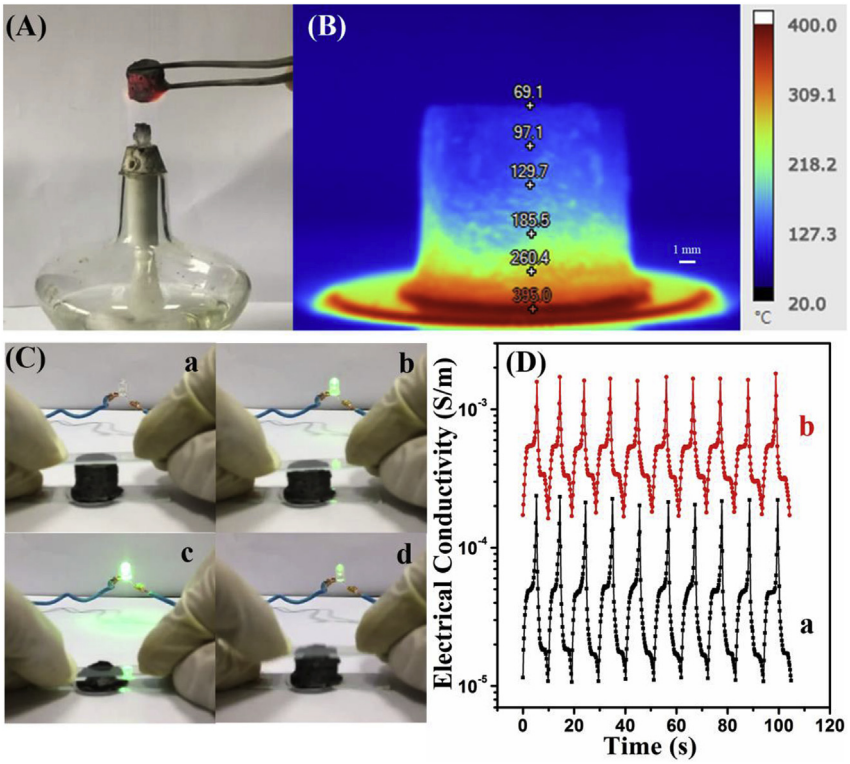

Fig. 3. (A) Photograph of Graphene Aerogel in a hot flame of an alcohol burner. (B) Infrared image of Graphene Aerogel on a 400 °C heating stage for 1 h, exhibiting a distinct temperature gradient and a relative low temperature of ~69 °C on the top surface of Graphene Aerogel. (C) Snapshots of the brightness of the lamp upon (a–c) compressing and (d) releasing the aerogel, which is series connected with aerogel in a circuit. (D) The strain-responsive volume electrical conductivity curves of (a) RGO Aerogel and (b) Graphene Aerogel for 10 cycles. (A colour version of this figure can be viewed online.)

$$\sigma = \frac{L}{RS} \quad (1)$$

where σ is volume electrical conductivity, R is the volume resistance (piezoresistance), L and S are the height and crossing-sectional area of the cylinder, and the results were displayed in Fig. 3D and Fig. S5. For RGO Aerogel and Graphene Aerogel, the strain-responsive volume electrical conductivity exhibits excellent compression reproducibility. Such reversible strain-responsive consistency can be maintained over 10, whereas no apparent creep behavior in electrical conductivity occurs in the whole compression cycles. In addition, as shown in Fig. S5, it can be obviously observed that the electrical conductivity of the aerogels will gradually increase with increasing the compression strain, while it will also gradually decrease and completely recover to the original state after releasing strain, exhibiting a nonlinear reversible strain-responsive behavior, which is similar to that of porous graphene/TPU foams [38,39]. Meanwhile, it is worthy to note that the change in electrical conductivity shows approximately one order of magnitude increase as the compression strain increases from 0% to 75%, indicating high sensitivity as a large-scale strain sensor. As the compressive strain is up to 75%, the electrical conductivity of RGO Aerogel starts to reach a highest value, which can be comparative with that of Graphene Aerogel. The large evolution in the volume electrical conductivity can be ascribed to the construction of 3D conducting paths under different compression strains. When compression stress is applied to the interconnected porous graphene aerogels, the entrapped air is extruded out as shown in Movie S4, thereby leading to the shrinking of the 3D conductive graphene network and the decrease of free space entangled in the network. As a result, the cell walls of internal microcellular structures (as shown in Fig. 1E) will start to contact with the adjacent one and more compact conductive pathways will be formed, yielding a dramatic increase in volume electrical conductivity. In contrast, once the compression stress is released, the volume electrical conductivity of the aerogels will gradually recover to the original state as air is drawn in again. Moreover, the volume electrical conductivity of Graphene Aerogel exhibits at least one order magnitude enhancement as compared to that of RGO Aerogel under the same compression strain, which once again confirms the efficiency in reduction of RGO during the thermal annealing process.

3.4. *Microwave absorption properties of RGO Aerogel and Graphene Aerogel under different compressive strains*

As a kind of large-scale strain sensor with high sensitivity in electrical conductivity, the formed interconnected 3D porous graphene network combined with excellent reversible compressibility can promote the aerogel to become a potential self-adjustable absorbent for attenuating the undesired electromagnetic wave. In order to further examine the effect of interconnected 3D porous graphene network under different compression strains on the microwave absorption performance of the aerogels, the paraffin was employed as a supporting matrix to immobilize the aerogel under certain compression strain, and the electromagnetic parameters of the aerogels with different compression strains from 0% to 10%, 30%, 50% and 75% were measured on a vector network analyzer (Agilent 8720ET) by using the coaxial wire method in the frequency range of 0.5–18 GHz. As displayed in Fig. 4 and Fig. S6, the relative permittivity and dielectric loss tangent (Tan $\delta_\varepsilon = \varepsilon''/\varepsilon'$) of the aerogels simultaneously show obvious frequency dependence and a

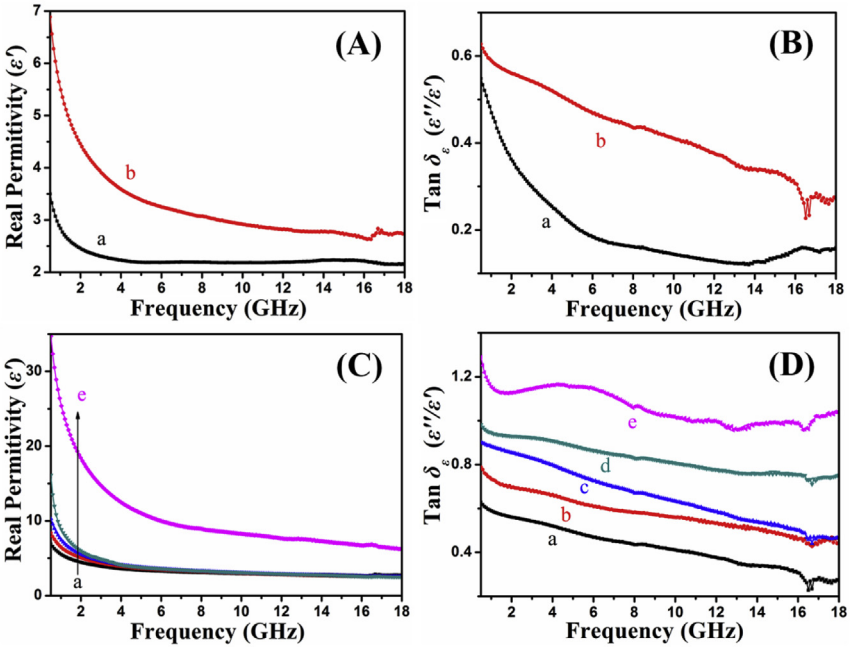

Fig. 4. (A) Frequency dependence of real permittivity and (B) dielectric loss tangent (Tan $\delta_\varepsilon = \varepsilon''/\varepsilon'$) of (a) uncompressed RGO Aerogel and (b) Graphene Aerogel in the range of 0.5–18 GHz; (C, D) the corresponding parameters for the Graphene Aerogels under a compressive strain of (a) 0%, (b) 10%, (c) 30%, (d) 50% and (e) 75%. (A colour version of this figure can be viewed online.)

nonlinear tendency to gradually increase as the applied compression strain increases, which agrees well with the results of strain-responsive volume electrical conductivity as shown in Fig. 3D. Furthermore, the corresponding parameters of Graphene Aerogel under different compression strains show a more significant enhancement as compared to those of RGO Aerogel as shown in Fig. 4A and B, which once again confirms the efficiency of the thermal reduction.

To study the microwave absorption performance of the aerogels under different compression strains, the reflection loss (*RL*) of incident electromagnetic wave was calculated on the basis of electromagnetic data by transmission line theory, Equations (2) and (3):

$$RL = 20\log\left|\frac{Z_{in}-1}{Z_{in}+1}\right| \tag{2}$$

$$Z_{in} = \sqrt{\frac{\mu_r}{\varepsilon_r}}\tanh\left[j\frac{2\pi fd\sqrt{\mu_r\varepsilon_r}}{c}\right] \tag{3}$$

where μ_r and ε_r were the measured relative complex permeability and permittivity, respectively, c was the speed of light, f was the frequency of microwaves and d was the thickness of the absorber. And the results are displayed in Fig. 5A and B. It can be clearly observed that the microwave absorption performance of the original Graphene Aerogel exhibits a distinct improvement in comparison with the uncompressed RGO Aerogel.

As shown in Fig. 5B(a), for original Graphene Aerogel, the qualified frequency bandwidth of microwave absorption (RL < −10 dB) is up to 3.16 GHz from 5.48 to 8.64 GHz. The excellent microwave absorption performance can be attributed to the enhanced electrical conductivity from RGO Aerogel to Graphene Aerogel after thermal reduction process. For the interconnected porous graphene network, the microcellular configuration with free space brings a large internal interface area as shown in Fig. 1E. Due to the impedance mismatching between air and graphene sheets, electromagnetic wave entering the aerogels would be reflected at the corresponding interface. Due to the existence of the closed microcellular structure, the random multiple reflection of electromagnetic wave would repeatedly occur at the internal interfaces of the cell wall as schematized in Fig. 5C, leading to the transfer of electromagnetic energy to be dissipated as heat, thereby realizing the efficient absorption of electromagnetic wave [40,41]. However, for RGO Aerogel, the lower real permittivity as shown in Fig. 4A would result in less backscattered microwave according to the Weston's theorem [42]. Although the real permittivity of the RGO Aerogel can be effectively enhanced with increasing the compression strain as displayed in Fig. S6A, the proportionate compression in the thickness still leads to the penetration of most incident microwave through the whole RGO Aerogel, thereby exhibiting unsatisfying absorption performance (RL > −10 dB) as shown in Fig. 5A. As for Graphene Aerogel, the higher dielectric loss (Fig. 4B) would bring a stronger conductive dissipation of electromagnetic waves as time dependent electromagnetic fields-induced currents occur on the conductive graphene network of aerogels [40]. Meanwhile, the effective enhancement in the real permittivity after thermal annealing process would also contribute to further improvement in the degree of impedance mismatching between air and graphene sheets, resulting in more back microwave reflection/scattering rather than penetration, which boosts the random multiple reflection of electromagnetic wave among the microcellular free spaces. As a consequence, the synergistic effect of conductive dissipation and random multiple reflection commonly promotes the effective enhancement in the microwave absorption performance of Graphene Aerogel as shown in Fig. 5B(a).

More interestingly, with increasing the compression strain, the microwave absorption peak of Graphene Aerogel continuously shifts toward higher frequency and exhibits a significant tendency to gradually increase and then decline in intensity and bandwidth as shown in Fig. 5B, which is in vivid contrast to the spiritless RGO Aerogel. With the applied compression strain increasing from 0% to 10%, 30%, 50%, and 75%, the maximum |*RL*| value of Graphene

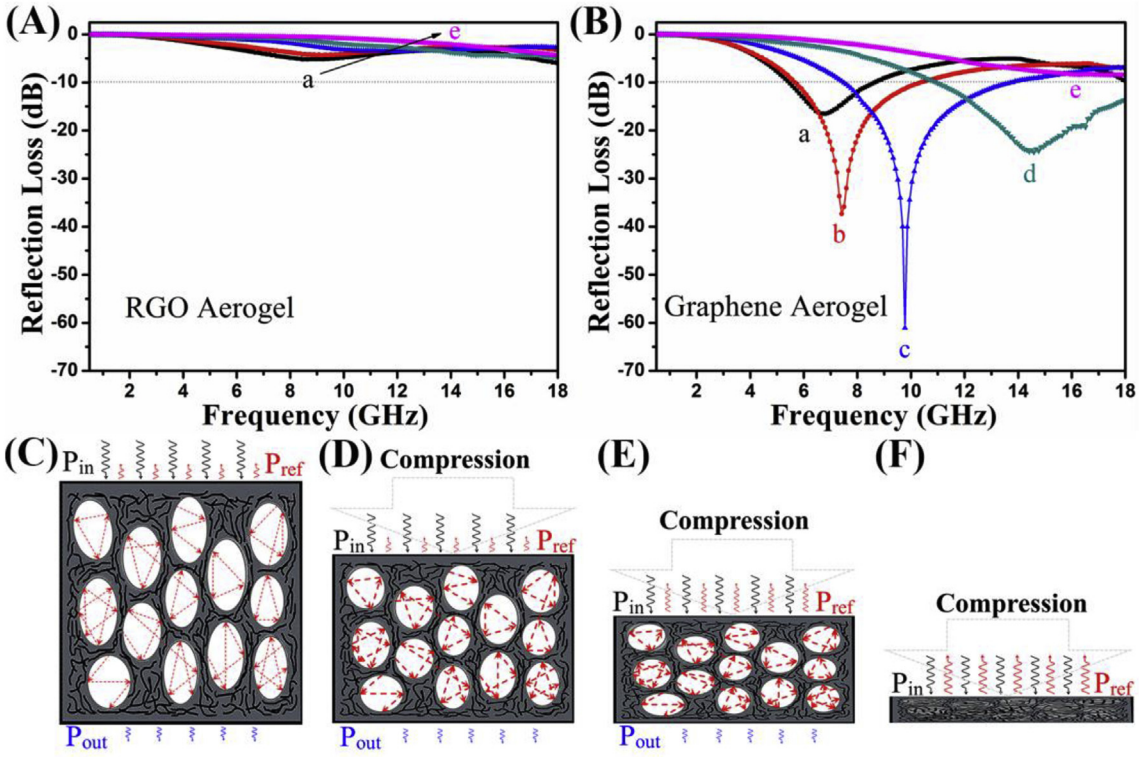

Fig. 5. (A, B) Microwave reflection loss curves of RGO Aerogel (6.91 mm) and Graphene Aerogels (6.87 mm) under a compressive strain of (a) 0%, (b) 10%, (c) 30%, (d) 50% and (e) 75% in the frequency range of 0.5–18 GHz. (C–F) Schematic representation of the microwave absorption mechanism for the Graphene Aerogel under different compression strains. (A colour version of this figure can be viewed online.)

Aerogel increases from 16.59 dB to 37.33 dB, 61.09 dB, and then decreases to 24.51 dB, and final 8.47 dB. Meantime, the qualified bandwidth also demonstrates a prominent enhancement from 3.16 GHz to 4.68 GHz, 6.30 GHz, 7.00 GHz and a subsequent decline to 0 GH. The conspicuous evolution in microwave absorption performance can be mainly attributed to the shrinking of interconnected 3D conductive graphene network under compression strain condition. With increasing the applied compression strain amplitude, the continuously increased dielectric loss (Fig. 4D) of Graphene Aerogel would effectively facilitate the conductive dissipation of electromagnetic waves. Moreover, it also brings more backscattering due to the enhancement in the real permittivity under compression (Fig. 4C). However, the shrinking of the 3D porous architecture would lower the internal free space, leading to the decrease of internal interface area, which will further weaken the random multiple reflections of electromagnetic wave among the cell wall. As a result, the final microwave absorption performance is determined by the enhancement of conductive dissipation and back microwave scattering, and the reduction of internal free space. At the initial stage (10%–30%) of compression strain, the positive enhancement of back microwave scattering plays a more important role than negative reduction of internal free space in the random multiple reflections of electromagnetic wave. As a result, the increased random multiple reflections and conductive dissipation will synergistically promote the effective absorption of incident electromagnetic waves as demonstrated in Fig. 5D. However, with increasing the compression strain (to 50%) as shown in Fig. 5E, further reduction of internal free space substantially weakens the random multiple reflections. Meanwhile, further enhancement of backscattering would result in more incident electromagnetic waves being reflected outside the aerogel, thereby impairing the effective absorption of incident electromagnetic waves (Fig. 5B(d)). When the sample is compressed completely (75%), the free space of the aerogel is fully extruded out (Fig. 5F). Meantime, the compact stacking contact of graphene network would bring more backscattering, which hinders the entrance of incident electromagnetic waves into the sample, exhibiting an inferior microwave absorption performance as demonstrated in Fig. 5B(e). Therefore, we can conclude that the effective construction of interconnected 3D porous conductive graphene network with high compressibility will contribute to realize the self-adjustment of microwave absorption performance through a simple mechanical compression rather than renewedly preparing a sample with big thickness or unhandily stacking the thin sample to form a thicker one.

Furthermore, to more comprehensively evaluate the thickness effect of RGO Aerogel and Graphene Aerogel under different compression strain configuration on the final microwave absorption performance, the 3D representations of reflection loss versus frequency (0.5–18 GHz) and thickness (1.00–5.00 mm) were calculated and shown in Fig. 6 and S7, which were also summarized in Fig. S8 and S9. As shown in Fig. S7 and S8, the proportionate compression in the thickness still leads to the penetration of most incident microwave through the whole RGO Aerogel due to the low electrical conductivity and permittivity, thereby exhibiting unsatisfying absorption performance ($RL > -10$ dB). As the compressive strain is up to 75%, the electrical conductivity and permittivity of RGO Aerogel start to reach a higher value, which is comparable to that of Graphene Aerogel as shown in Figs. 3D and 4. As shown in Fig. S7D and S8D, the microwave absorption performance of RGO Aerogel can be gradually enhanced by increasing the thickness of RGO Aerogel under a compressive strain of 75%. However, the complete compressed RGO Aerogel sacrifices its compressibility to elevate its electrical conductivity and permittivity, thereby losing

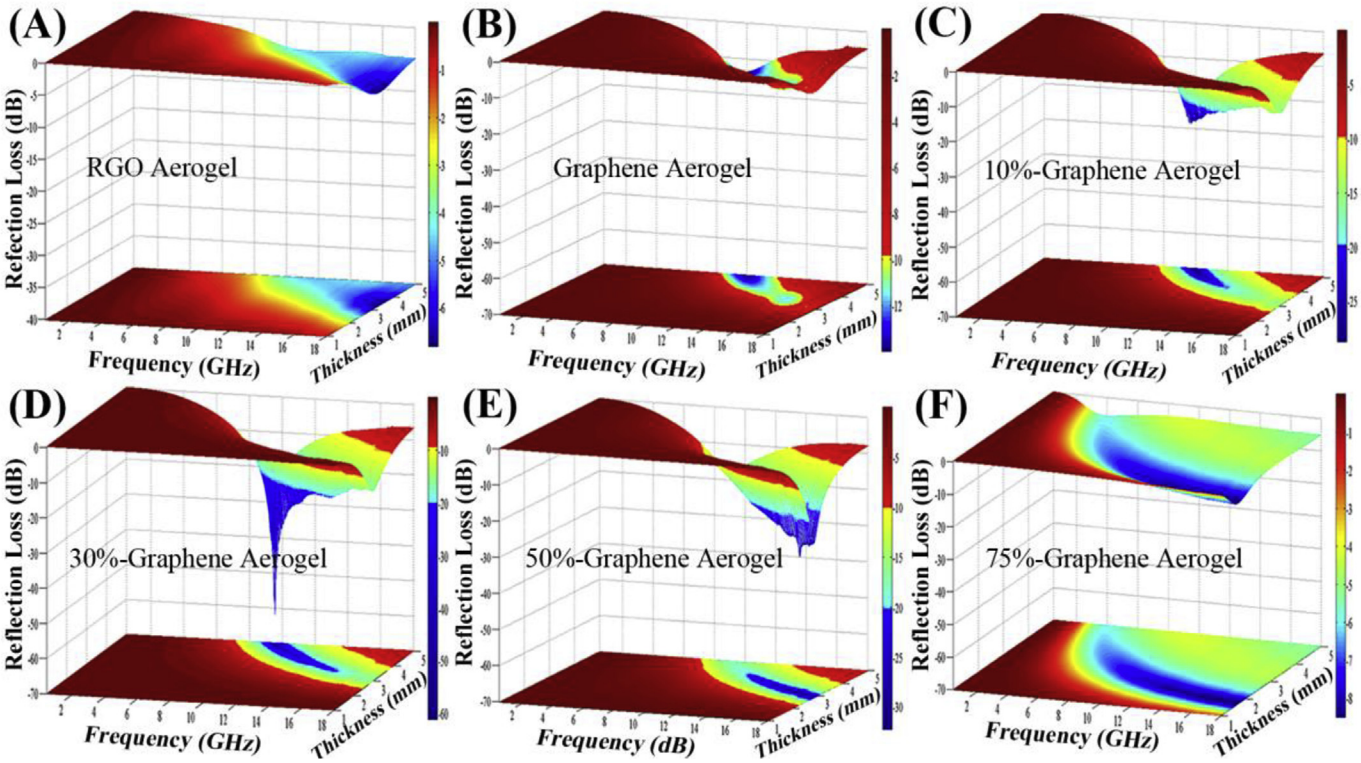

Fig. 6. Three-dimensional reflection loss of (A) uncompressed RGO Aerogel and Graphene Aerogels under a compressive strain of (B) 0%, (C) 10%, (D) 30%, (E) 50% and (F) 75%. (A colour version of this figure can be viewed online.)

the self-adjustment in microwave absorption. Therefore, further thermal annealing process for RGO Aerogel is indispensable to further elevate its electrical conductivity and permittivity, thereby realizing the self-adjustment in microwave absorption performance. For Graphene Aerogel, as shown in Fig. 6 and S9, it also exhibits a similar tendency to gradually increase and then decline with the applied compression strain rising. More importantly, absorption performance of Graphene Aerogel exhibits a remarkable enhancement with changing the thickness of the samples under a certain compression strain configuration. It is worth noting that when the compression strain of the sample is controlled to be 30% with a thickness of 4.81 mm, Graphene Aerogel can achieve its optimal absorbing value of 61.09 dB with a broad qualified bandwidth of 6.30 GHz. In comparison with other graphene-based microwave absorbing materials as displayed in Table 1, for this study, the facile, low-cost and large-scale approach to construct the macroscopic free-standing all-graphene 3D architecture and excellent broadband microwave absorption performance combined with ultralight density and controllable thickness make it possible for Graphene Aerogel to become an effective microwave attenuation material with a great potential to be deployed in aerospace and aviation fields.

4. Conclusions

Macroscopic 3D free-standing porous all-graphene aerogel with large internal free space was successfully fabricated through a mild in-situ self-assembly and thermal annealing processes. The results of SEM, TGA, UV–vis, XPS, Roman, and XRD confirmed that in-situ self-assembly and thermal annealing processes can effectively promote the reduction of GO and the restoration of π-conjugated network within graphene sheets, leading to enhancement of π-π interaction between adjacent graphene sheets, which facilitates the formation of interconnected 3D porous graphene network with ultralow density. Meanwhile, the growth of ice crystals during the freeze-drying process will further push the adjacent reduced graphene oxide sheets to form a microcosmic stacking structure as the cell wall of microcellular cavity, thereby endowing the 3D

Table 1
Microwave absorption performance in the recently reported graphene-based materials.

	Content (wt%)	Thickness (mm)	Frequency range [GHz] ($RL < -10$ dB)	Qualified Bandwidth (GHz)	Max|RL| (dB)	Refs
FeCoB/graphene/PI	1	2	10.2–15	4.8	31	[15]
TRGN-2	1	3.5	9.36–16.83	7.47	44.5	[18]
3D-PPy/RGO	10	3.0	10.2–16.96	6.76	54.4	[17]
RGO/ZnO in wax	15	2.4	11.4–18	6.7	54.2	[13]
$NiFe_2O_4$@graphene@CuS	20	2.5	9.7–14.2	4.5	54.5	[14]
NiO@graphene in wax	25	1.7	12.48–16.72	4.24	59.6	[7]
CoS_2/rGO	50	2.2	9.1–13.2	4.1	56.9	[6]
Graphene foam	1.4 mg/cm^3	10	4.1–18	13.9	30.5	[20]
Graphene foam	1.6 mg/cm^3	10	3.7–18	14.3	34.0	[43]
30%-Graphene Aerogel	6.8 mg/cm^3	4.81	7.5–13.8	6.30	61.09	This work

(PI: Polyimide; TRGN: Thermally reduced graphene networks; PPy: Polypyrrole).

architecture with excellent mechanical compressibility. As a consequence, the high thermally stable all-graphene composition and large porosity of aerogels made it possible to quickly remove heat during combustion, exhibiting a conspicuous fire-retardancy. Moreover, excellent recoverable compressibility with high strain levels of up to 75% endowed the aerogel with high sensitive strain-responsive characteristic, thereby opening a new way for realizing the self-adjustment of internal free space and electrical conductivity of 3D architecture. Based on these results, the microwave absorption performance of the Graphene Aerogel can be effectively tuned via a simple mechanical compression. The optimal absorbing value was up to 61.09 dB with a broad qualified bandwidth of 6.30 GHz at a thickness of 4.81 mm when the compression strain of the sample was controlled to be 30%.

Acknowledgements

The financial support from National Natural Science Foundation of China (Project No. 51603029, No. 51403029) is gratefully acknowledged.

Appendix A. Supplementary data

Supplementary data related to this article can be found at https://doi.org/10.1016/j.carbon.2018.08.014.

References

[1] D. Ding, Y. Wang, X.D. Li, R. Qiang, P. Xu, W.L. Chu, et al., Rational design of core-shell Co@C microspheres for high-performance microwave absorption, Carbon 111 (2017) 722–732.
[2] M.S. Cao, J. Yang, W.L. Song, D.Q. Zhang, B. Wen, H.B. Jin, et al., Ferroferric oxide/multiwalled carbon nanotube vs polyaniline/ferroferric oxide/multiwalled carbon nanotube multiheterostructures for highly effective microwave absorption, ACS Appl. Mater. Interfaces 4 (12) (2012) 6949–6956.
[3] H. Sun, R.C. Che, X. You, Y.S. Jiang, Z.B. Yang, J. Deng, et al., Cross-stacking aligned carbon-nanotube films to tune microwave absorption frequencies and increase absorption intensities, Adv. Mater. 26 (48) (2014) 8120–8125.
[4] B. Zhao, J.H. Deng, R. Zhang, L.Y. Liang, B.B. Fan, Z.Y. Bai, et al., Recent advances on the electromagnetic wave absorption properties of Ni based materials, Eng. Sci. (2018). https://doi.org/10.30919/es8d735 (in press).
[5] P.T. Xie, B. He, F. Dang, J. Lin, R.H. Fan, C.X. Hou, et al., Bio-gel derived nickel/carbon nanocomposites with enhanced microwave absorption, J. Mater. Chem. C (2018), https://doi.org/10.1039/C8TC02127A (in press).
[6] C. Zhang, B.C. Wang, J.Y. Xiang, C. Su, C.P. Mu, F.S. Wen, Z.Y. Liu, Microwave absorption properties of CoS_2 nanocrystals embedded into reduced graphene oxide, ACS Appl. Mater. Interfaces 9 (34) (2017) 28868–28875.
[7] L. Wang, H.L. Xing, S.T. Gao, X.L. Jia, Z.Y. Shen, Porous flower-like NiO@graphene composites with superior microwave absorption properties, J. Mater. Chem. C 5 (2017) 2005–2014.
[8] L. Wang, Y. Huang, X. Sun, H.J. Huang, P.B. Liu, M. Zong, Y. Wang, Synthesis and microwave absorption enhancement of graphene@Fe_3O_4@SiO_2@NiO nanosheet hierarchical structures, Nanoscale 6 (2014) 3157–3164.
[9] L. Wang, Y. Huang, C. Li, X. Sun, Hierarchical graphene@Fe_3O_4 nanocluster @carbon@MnO_2 nanosheet array composites: synthesis and microwave absorption performance, Phys. Chem. Chem. Phys. 17 (2015) 5878–5886.
[10] V.K. Singh, A. Shukla, M.K. Patra, L. Saini, R.K. Jani, S.R. Vadera, Microwave absorbing properties of a thermally reduced graphene oxide/nitrile butadiene rubber composite, Carbon 50 (6) (2012) 2202–2208.
[11] G.S. Wang, X.J. Zhang, Y.Z. Wei, S. He, L. Guo, M.S. Cao, Polymer composites with enhanced wave absorption properties based on modified graphite and polyvinylidene fluoride, J. Mater. Chem. 1 (2013) 7031–7036.
[12] X.J. Zhang, G.S. Wang, Y.Z. Wei, L. Guo, M.S. Cao, Polymer-composite with high dielectric constant and enhanced absorption properties based on graphene-CuS nanocomposites and polyvinylidene fluoride, J. Mater. Chem. 1 (2013) 12115–12122.
[13] W. Feng, Y.M. Wang, J.C. Chen, L. Wang, L.X. Guo, J.H. Ouyang, et al., Reduced graphene oxide decorated with in-situ growing ZnO nanocrystals: facile synthesis and enhanced microwave absorption properties, Carbon 108 (2016) 52–60.
[14] P.B. Liu, Y. Huang, J. Yan, Y.W. Yang, Y. Zhao, Construction of CuS Nanoflakes vertically aligned on magnetically decorated graphene and their enhanced microwave absorption properties, ACS Appl. Mater. Interfaces 8 (8) (2016) 5536–5546.
[15] Z.J. Xia, J. He, X.L. Ou, Y. Li, Y. Wang, B. Shen, et al., Enhanced microwave-absorption performance of FeCoB/Polyimide-Graphene composite by electric field modulation, Compos. Sci. Technol. 152 (2017) 222–230.
[16] X.J. Zhang, G.S. Wang, W.Q. Cao, Y.Z. Wei, J.F. Liang, L. Guo, M.S. Cao, Enhanced microwave absorption property of reduced graphene oxide (RGO)-$MnFe_2O_4$ nanocomposites and polyvinylidene fluoride, ACS Appl. Mater. Interfaces 6 (10) (2014) 7471–7478.
[17] F. Wu, A.M. Xie, M.X. Sun, Y. Wang, M.Y. Wang, Reduced graphene oxide (RGO) modified spongelike polypyrrole (PPy) aerogel for excellent electromagnetic absorption, J. Mater. Chem. 3 (2015) 14358–14369.
[18] W.W. Liu, H. Li, Q.P. Zeng, H.N. Duan, Y.P. Guo, X.F. Liu, C.Y. Sun, H.Z. Liu, Fabrication of ultralight three-dimensional graphene networks with strong electromagnetic wave absorption properties, J. Mater. Chem. 3 (2015) 3739–3747.
[19] B. Shen, Y. Li, D. Yi, W.T. Zhai, X.C. Wei, W.G. Zheng, Microcellular graphene foam for improved broadband electromagnetic interference shielding, Carbon 102 (2016) 154–160.
[20] Y. Zhang, Y. Huang, T.F. Zhang, H.C. Chang, P.S. Xiao, H.H. Chen, et al., Broadband and tunable high-performance microwave absorption of an ultralight and highly compressible graphene foam, Adv. Mater. 27 (12) (2015) 2049–2053.
[21] D.C. Marcano, D.V. Kosynkin, J.M. Berlin, A. Sinitskii, Z.Z. Sun, A. Slesarev, et al., Improved synthesis of graphene oxide, ACS Nano 4 (8) (2010) 4806–4814.
[22] I.K. Moon, S. Yoon, K.Y. Chun, J. Oh, Highly elastic and conductive n-doped monolithic graphene aerogels for multifunctional applications, Adv. Funct. Mater. 25 (45) (2015) 6976–6984.
[23] J.H. Li, J.Y. Li, H. Meng, S.Y. Xie, B.W. Zhang, L.F. Li, et al., Ultra-light, compressible and fire-resistant graphene aerogel as a highly efficient and recyclable absorbent for organic liquids, J. Mater. Chem. 2 (2014) 2934–2941.
[24] H.Y. Sun, Z. Xu, C. Gao, Multifunctional, ultra-flyweight, synergistically assembled carbon aerogels, Adv. Mater. 25 (18) (2013) 2554–2560.
[25] L. Qiu, J.Z. Liu, S.L.Y. Chang, Y.Z. Wu, D. Li, Biomimetic superelastic graphene-based cellular monoliths, Nat. Commun. 3 (2012) 1241.
[26] K.H. Kim, Y. Oh, M.F. Islam, Graphene coating makes carbon nanotube aerogels superelastic and resistant to fatigue, Nat. Nanotechnol. 7 (2012) 562–566.
[27] Y.Q. Guo, G.J. Xu, X.T. Yang, K.P. Ruan, T.B. Ma, Q.Y. Zhang, et al., Significantly enhanced and precisely modeled thermal conductivity in polyimide nanocomposites by chemically modified graphene via in-situ polymerization and electrospinning-hot press technology, J. Mater. Chem. C 6 (2018) 3004–3015.
[28] J.I. Paredes, S. Villar-Rodil, A. Martínez-Alonso, J.M.D. Tascón, Graphene oxide dispersions in organic solvents, Langmuir 24 (19) (2008) 10560–10564.
[29] D. Li, M.B. Müller, S. Gilje, R.B. Kaner, G.G. Wallace, Processable aqueous dispersions of graphene nanosheets, Nat. Nanotechnol. 3 (2008) 101–105.
[30] X.D. Wang, X.H. Liu, H.Y. Yuan, H. Liu, C.T. Liu, T.X. Li, et al., Non-covalently functionalized graphene strengthened poly(vinyl alcohol), Mater. Des. 139 (2018) 372–379.
[31] K.N. Kudin, B. Ozbas, H.C. Schniepp, R.K. Prudhomme, I.A. Aksay, R. Car, Raman spectra of graphite oxide and functionalized graphene sheets, Nano Lett. 8 (1) (2008) 36–41.
[32] G.P. Jiang, M. Goledzinowski, F.J.E. Comeau, H. Zarrin, G. Lui, J. Lenos, et al., Free-standing functionalized graphene oxide solid electrolytes in electrochemical gas sensors, Adv. Funct. Mater. 26 (11) (2016) 1729–1736.
[33] Y.Y. Li, T. Jing, G.F. Xu, J.Z. Tian, M.Y. Dong, Q. Shao, et al., 3-D magnetic graphene oxide-magnetite poly(vinyl alcohol) nanocomposite substrates for immobilizing enzyme, Polymer 149 (1) (2018) 13–22.
[34] H.Q. Sun, S.Z. Liu, G.L. Zhou, H.M. Ang, M.O. Tadé, S.B. Wang, Reduced graphene oxide for catalytic oxidation of aqueous organic pollutants, ACS Appl. Mater. Interfaces 4 (11) (2012) 5466–5471.
[35] Y.D. Zhang, P.Y. Zhu, L.L. Huang, J. Xie, S.C. Zhang, G.S. Cao, X.B. Zhao, Few-layered SnS_2 on few-layered reduced graphene oxide as na-ion battery anode with ultralong cycle life and superior rate capability, Adv. Funct. Mater. 25 (3) (2015) 481–489.
[36] J.H. Yang, Y.J. Gao, W. Zhang, P. Tang, J. Tan, A.H. Lu, D. Ma, Cobalt phthalocyanine-graphene oxide nanocomposite: complicated mutual electronic interaction, J. Phys. Chem. C 117 (8) (2013) 3785–3788.
[37] H.L. Wang, X. Zhang, N. Wang, Y. Li, X. Feng, Y. Huang, et al., Ultralight, scalable, and high-temperature-resilient ceramic nanofiber sponges, Sci Adv 3 (6) (2017), e1603170.
[38] H. Liu, M.Y. Dong, W.J. Huang, J.C. Gao, K. Dai, J. Guo, et al., Lightweight conductive graphene/thermoplastic polyurethane foams with ultrahigh compressibility for piezoresistive sensing, J. Mater. Chem. C 5 (2017) 73–83.
[39] H. Liu, Y.L. Li, K. Dai, G.Q. Zheng, C.T. Liu, C.Y. Shen, et al., Electrically conductive thermoplastic elastomer nanocomposites at ultralow graphene loading levels for strain sensor applications, J. Mater. Chem. C 4 (2016) 157–166.
[40] Z. Fang, C. Li, J. Sun, H. Zhang, J. Zhang, The electromagnetic characteristics of carbon foams, Carbon 45 (2007) 2873–2879.
[41] J. Guo, H.X. Song, H. Liu, C.J. Luo, Y.R. Ren, T. Ding, et al., Polypyrrole -interface-functionalized nano-magnetite epoxy nanocomposites as electromagnetic wave absorbers with enhanced flame retardancy, J. Mater. Chem. C 5 (2017) 5334–5344.
[42] X. Cao, Y. Shi, W. Shi, G. Lu, X. Huang, Q. Yan, et al., Preparation of novel 3D graphene networks for supercapacitor applications, Small 7 (22) (2011) 3163–3168.
[43] Y. Zhang, Y. Huang, H.H. Chen, Z.Y. Huang, Y. Yang, P.S. Xiao, et al., Composition and structure control of ultralight graphene foam for high-performance microwave absorption, Carbon 105 (2016) 438–447.